

Engineering the Near-Edge Electronic Structure of SnSe through Strains

Yabei Wu,^{1,2} Weiyi Xia,² Weiwei Gao,² Wei Ren,^{1,*} and Peihong Zhang^{1,2,†}

¹*International Centre for Quantum and Molecular Structures, Materials Genome Institute and Department of Physics, Shanghai University, 99 Shangda Road, Shanghai 200444, China*

²*Department of Physics, University at Buffalo, State University of New York, Buffalo, New York 14260, USA*

(Received 29 April 2017; revised manuscript received 24 July 2017; published 11 September 2017)

The discovery of the unprecedented figure of merit ZT of SnSe has sparked a large number of studies on the fundamental physics of this material and further improvement through guided materials design and optimization. Motivated by its rich chemical-bonding characters, unusual multivalley electronic structure, and the sensitivity of the band-edge states to lattice strains, we carry out accurate quasiparticle calculations for the low-temperature phase SnSe under strains. We illustrate how the band-edge states can be engineered by lattice strains, including the size and the nature of the band gap, the positions of the band extrema in the Brillouin zone, and the control of the number of electron and/or hole valleys. The distinct atomic origin and orientation of the wave functions of the different band-edge states dictates the relative shift in their band energy, enabling active control of the near-edge electronic structure of this material. Our work demonstrates that strain engineering is a promising way to manipulate the low-energy electronic structure of SnSe, which can have profound influences on the optical and transport properties of this material.

DOI: 10.1103/PhysRevApplied.8.034007

I. INTRODUCTION

As one of the most promising candidates for thermoelectric applications [1–4], tin selenide (SnSe) has recently attracted much research interest. This material displays the highest thermoelectric figure of merit ZT without doping [2,3], and, importantly, its composition is earth-abundant and nontoxic. SnSe crystallizes in a low-temperature (LT) phase [Fig. 1(a)] with the $Pnma$ space group under ambient conditions and undergoes a second-order phase transition to a high-temperature (HT) phase [Fig. 1(b)] with the $Cmcm$ space group at about 750–800 K [2]. Both the $Cmcm$ and $Pnma$ phases have layered structures, in which the intra-layer bonds are much stronger than interlayer interactions.

In spite of its impressive performance, the record-high ZT value of 2.6 is achieved only at above 800 K [2]. At room temperature, the ZT value is less than 0.5 [2]. This greatly limits the potential applications of SnSe-based thermoelectric devices. Compared with the LT phase, the HT $Cmcm$ phase has a lower lattice thermal conductivity, which may be attributed to the greater phonon anharmonicity in the HT phase [5,6]. Moreover, the smaller band gap of the $Cmcm$ phase ($E_g^{Cmcm} = 0.54$ eV, to be compared with $E_g^{Pnma} = 0.86$ eV) leads to an increase of the electrical conductivity σ by one order of magnitude as the temperature changes from 500 to 800 K [2]. The large variation of phonon and electronic properties evidently stems from the structural difference between the two phases.

In order to further optimize the performance and extend the range of the working temperature of SnSe, several approaches have been explored, for example, hole doping [1], applying hydrostatic pressure [7,8], and nanostructuring [9,10]. Another important alternative is strain engineering, which has long been used as an effective and predictable means for tuning the materials properties [11–16], including strain-induced structural phase transitions [17–19], indirect-direct band-gap transition [11–13], and semiconductor-metal transition [12,20]. Previous work [4,21,22] also demonstrated the possibility of applying strains to tune the thermoelectric power factor. The band edges of SnSe have several competing local extrema within a small energy window, and the wave functions of the electronic states near these local extrema have different atomic origins. These states may respond differently to various types of strain, enabling an effective means for engineering the electronic structure of this material.

In this work, we present a detailed investigation on how the near-edge electronic structure and the quasiparticle band gap of the LT phase SnSe can be engineered using strains within density functional theory (DFT) [23] and the GW approximation [24–26]. Our results show that the band gap of the LT SnSe can be broadly tuned from 0 to 1.2 eV and from indirect to direct gap under strains. In particular, SnSe is predicted to undergo a semiconductor-metal transition under a biaxial compressive strain of 4% in the bc plane [lattice a , b , and c are defined in Fig. 1(a)]. More importantly, we find that strain can be used to control the number of electron and/or hole valleys in this material. Unlike modifying materials properties through chemical

*renwei@shu.edu.cn

†pzhang3@buffalo.edu

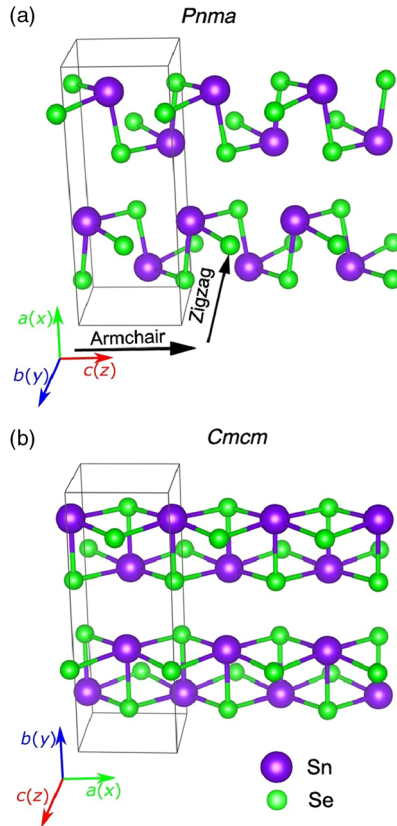


FIG. 1. Crystal structures of orthorhombic SnSe. (a) Low-temperature *Pnma* phase, (b) high-temperature *Cmcm* phase.

means, strain engineering enables the active control of materials properties. We mention that, although there have been previous DFT-based studies [21] of the strain effects on the electronic properties of SnSe, our *GW* results provide more accurate predictions which can be compared directly with experiments and guide future materials design.

II. COMPUTATIONAL DETAILS

The VASP package [27,28] is used for optimizing the crystal structures of the LT phase SnSe under various strains ranging from -8% (compressive) to 8% (tensile) and for computing the DFT band structures. The lattice parameters and atomic positions are fully relaxed within the constraint imposed by the strain. The generalized gradient approximation (GGA) [29] of Perdew-Burke-Ernzerhof (PBE) [30] is used for the DFT band-structure calculations. The Brillouin zone integration is carried out using a $3 \times 9 \times 9$ k grid.

Since SnSe assumes a layered structure, it is important that the van der Waals (vdW) interaction between layers is accurately captured in DFT calculations. We compare the performance of several methods, including the local density approximation (LDA) [31,32], GGA-PBE, DFT-D2 [33], and various vdW density functionals (vdW DFs), namely, optPBE [34], optB88 [34], and optB86b [35], for their

TABLE 1. Comparison between the experimental and calculated lattice parameters of bulk LT (*Pnma*) phase SnSe. Here a , b , and c are lattice constants defined in Fig. 1(a), $\Delta a/a$, $\Delta b/b$, and $\Delta c/c$ are the relative errors of the theoretical lattice constants, and d is the averaged absolute deviation of the atomic positions of the optimized structure compared with experiment.

Functional	a (Å)	$\Delta a/a$ (%)	b (Å)	$\Delta b/b$ (%)	c (Å)	$\Delta c/c$ (%)	d (Å)
LDA	11.334	-1.46	4.120	-0.79	4.324	-2.83	0.11
PBE	11.794	2.54	4.212	1.42	4.527	1.73	0.16
DF2	12.529	8.93	4.330	4.26	4.866	9.35	0.61
optPBE	11.916	3.60	4.240	2.09	4.563	2.54	0.23
optB88	11.809	2.67	4.229	1.83	4.488	0.85	0.16
optB86b	11.614	0.97	4.198	1.08	4.413	-0.83	0.07
Experiment [40]	11.502		4.153		4.450		

reliability in predicting the crystal structure of LT (*Pnma*) SnSe as shown in Table I. We find that the optB86b functional performs best in predicting both the lattice parameters and the internal atomic positions of SnSe. Hence, we use the optB86b functional for all structural optimizations. In this work, we focus on the evolution of electronic properties of the LT *Pnma* phase SnSe when it is subjected to uniaxial strain along the b (zigzag) and c (armchair) directions and biaxial strain in the bc plane.

Considering the fact that Sn is a rather heavy element, one might expect that the spin-orbital coupling (SOC) effects be important in this material. This is not the case here, however, due to the low symmetry of the system. The upper panel in Fig. 2 compares the PBE band structures of *Pnma* SnSe calculated with (shown in red) and without (shown in blue) including the SOC, which shows no noticeable SOC effects. We call this phenomenon *quenching of the SOC effect* due to the low symmetry of the structure. In other words, although the SOC potential $\Delta V_{\text{SOC}}^L(\vec{r})$ is large for Sn, the low symmetry of the structure removes the degeneracy of the electronic states (there are, however, still accidental degeneracy and near-degenerate states), resulting in vanishing SOC effects on the Kohn-Sham eigenvalue, i.e., $\langle \psi_{nk} | \vec{S} \cdot \vec{L} | \psi_{nk} \rangle \sim 0$. To better illustrate this point, we also carry out calculations for the high-symmetry rocksalt SnSe as shown in the lower panel in Fig. 2. As expected, the SOC effects are clearly seen for degenerate states (for example, at the Γ point). We mention that quenching of SOC has been discussed in the context of other symmetry-lowering mechanisms such as dynamical Jahn-Teller systems [36]. Therefore, we neglect SOC effects in *Pnma* SnSe in the following discussion.

The *GW* calculations are carried out using a local version of the BERKELEYGW package [37]. The Hybertsen-Louie generalized plasmon-pole (HL GPP) model [25] is used to extend the static dielectric matrix to finite frequencies. Although the *GW* approximation is recognized as one of

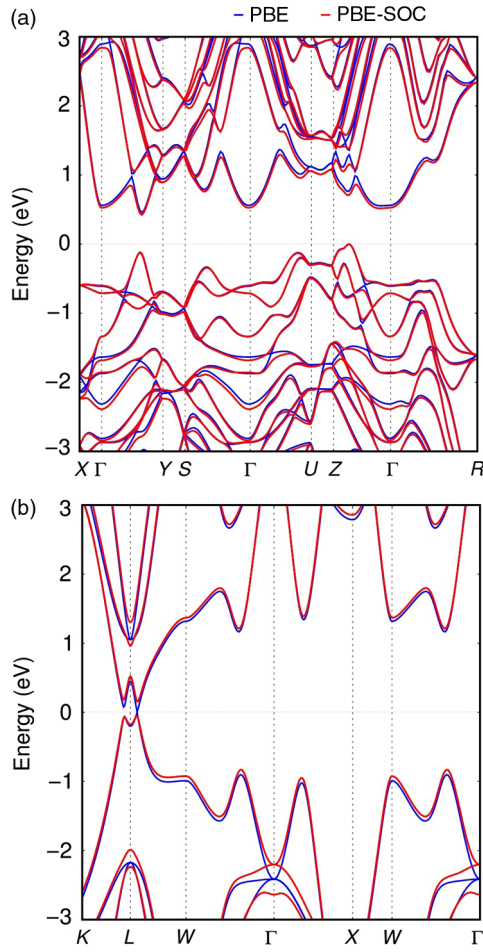


FIG. 2. Calculated band structures of SnSe with (shown in red) and without (shown in blue) including the spin-orbital coupling effect for the low-symmetry *Pnma* SnSe (upper panel) and high-symmetry rocksalt SnSe (lower panel).

the most accurate theories for predicting the quasiparticle properties of materials, large-scale *GW* calculations using the conventional approach are still very computationally expensive. Recently, we proposed an efficient energy-integration method [38] that can greatly speed up large-scale *GW* calculations without sacrificing the accuracy. This timely development enables fast and accurate predictions of the quasiparticle properties of SnSe under various strains. We carefully test the convergence of the *GW* results (to be discussed in more detail later) with respect to the k -point sampling, kinetic energy cutoff of dielectric matrices, and the number of conduction bands included in the dielectric function and self-energy calculations.

III. RESULTS AND DISCUSSION

A. Quasiparticle band structure of the unstrained LT *Pnma* phase SnSe

Figure 3 compares the DFT-PBE and *GW* band structures of the LT *Pnma* phase SnSe using the structure

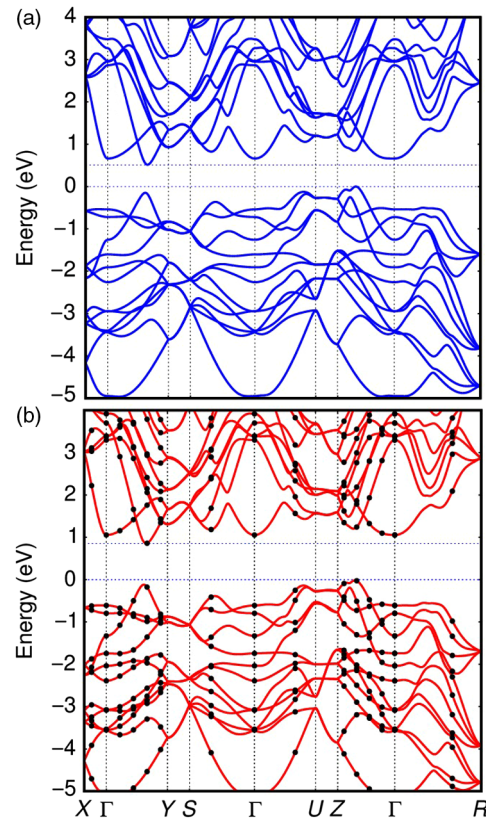


FIG. 3. Band structure of LT *Pnma* SnSe calculated using (a) the PBE functional and (b) the *GW* approximation. The black dots in (b) are the calculated *GW* energies, and red lines are the Wannier interpolated *GW* band structure.

relaxed with the optB86b-vdW functional. The valence-band maximum (VBM) is placed at zero in both plots. We employ the Wannier interpolation [39] method to generate the *GW* band structure using the results calculated on a $3 \times 9 \times 9$ uniform k grid. The PBE functional gives an indirect minimum gap of about 0.46 eV, and subsequent *GW* calculations predict a gap of 0.83 eV, which agrees rather well with the experimental band gap of 0.86 eV [2]. We mention that the calculated *GW* band gap is slightly larger (0.87 eV) if the experimental crystal structure [40] is used. The VBM is located between Z and Γ near $k = [0, 0, 1/3]$, and the conduction-band minimum (CBM) is located between Y and Γ near $k = [0, 1/3, 0]$. The band structure of SnSe has been discussed by several groups [3,41,42], and our results are consistent with previous ones.

An interesting feature of the band structure is the existence of several competing local extrema in the band edges that are within an energy window of 0.2 eV. Since these competing band-edge states are derived from different atomic states (shown in Fig. 4), they may respond differently to various type of strains, opening up the possibility of engineering the band-edge states via strains. For example, strain may induce an indirect-to-direct band gap and/or semiconductor-metal transitions, as we discuss later.

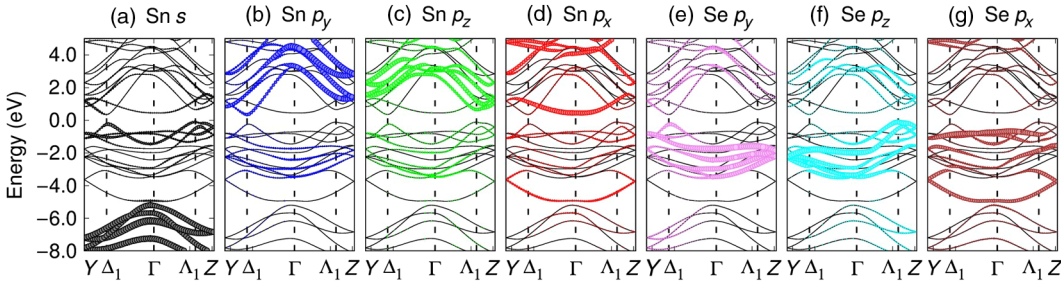


FIG. 4. Projected band structure of LT *Pnma* SnSe showing the distinct atomic characters of the low-energy valence and conduction states.

Sn 5*s*-derived states (the lone-pair states) lie around -8.5 to -5.5 eV (PBE result) but also contribute significantly to the top valence states through hybridization with Se 4*p* states [Fig. 4(a)]. In particular, the local maximum of the valence band along the Γ to Y direction (labeled Δ_1 in Fig. 4) shows a strong hybridization between the Sn *s* and the Se *p_y* orbitals [Figs. 4(a) and 4(e)]. The VBM state along the Γ to Z direction (labeled Λ_1 in Fig. 4), on the other hand, is a result of the hybridization between the Sn *s* and the Se *p_z* orbitals. (The definition of the Cartesian coordinates is shown in Fig. 1.) These two local maxima are very close in energy. When the system is under strain, their distinct wave-function characters lead to rather different behaviors, as we discuss later. The low-energy conduction bands are mainly derived from the Sn 5*p* states [Figs. 4(b)-4(d)], whereas the valence states from -5.0 to 0 eV are mostly of Se 4*p* character with some hybridization with Sn 5*s* and 5*p* states. Se 4*s* states lie at much lower energies (-13 to -12 eV) which are not shown in the figure.

B. Atomic-origin-dependent quasiparticle self-energy correction

Considering the different atomic characters of the valence and conduction states, it is not surprising that the *GW* self-energy correction depends strongly on the atomic origins of these states. Figure 5 shows the energy (and atomic-origin) -dependent *GW* correction $\Delta E_{nk}^{GW} = E_{nk}^{GW} - E_{nk}^{\text{DFT}}$. For simple materials such as Si or Ge, the *GW* quasiparticle corrections can sometimes be conveniently modeled with a scissors operator, which typically scales linearly with the band energy [25]. The situation is a little more complex here, since different atomic states may have, among other factors, different degrees of localization and, thus, different self-energy corrections. For example, Se 4*p* states are slightly more localized than the Sn 5*s* states. As a result, although the Se 4*p*-derived states are higher in energy, overall they have a greater self-energy correction as shown in Fig. 5. It is interesting that within each group of states (as indicated by the circles in the figure) the self-energy correction depends approximately linearly with the band energy. However, even within each group of states, the deviation of the *GW* correction from a simple linear scaling is still large (approximately ± 0.1 eV), stressing the importance of accurate *GW* calculations.

The distinct atomic characters of the band-edge states also give rise to different convergence behaviors of the *GW* results with respect to various cutoff parameters such as the kinetic energy cutoff (E_{cut}) for the dielectric matrix and the number of conduction bands (N_c) included in the *GW* calculations [43]. It is important to inspect the convergence behavior of the *GW* results, since underconverged results may lead to false predictions. Figure 6(a) shows the calculated *GW* band gap (minimum indirect gap) as a function of N_c and E_{cut} . It can be seen that a kinetic cutoff for the dielectric matrix of about 20 Ry (approximately 270 eV) is needed to converge the band gap to about 0.02 eV, and the number of bands required to converge the *GW* result is about 3000 (or 375 per atom). If a small E_{cut} of 5 Ry (approximately 70 eV) is used, the minimum gap is predicted to be only about 0.65 eV. Figure 6(b) shows similar convergence behavior for the direct gap at Γ .

In this work, we carry out *GW* calculations for about 20 strained structures. It would be extremely time consuming if the conventional method [25] were used. Recently, we developed an efficient integration method [38] that can drastically speed up fully converged *GW* calculations. Our method exploits the asymptotic behavior of the density of states of materials at high energies and approximates the summation over high-energy conduction bands in both

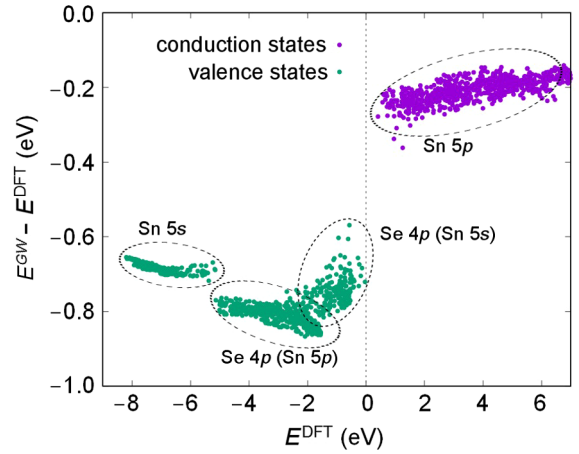


FIG. 5. Quasiparticle corrections to the Kohn-Sham DFT eigenvalues of LT *Pnma* SnSe. The distinct atomic-origin dependence of the self-energy correction is emphasized by circles indicating the primary atomic characters of the states.

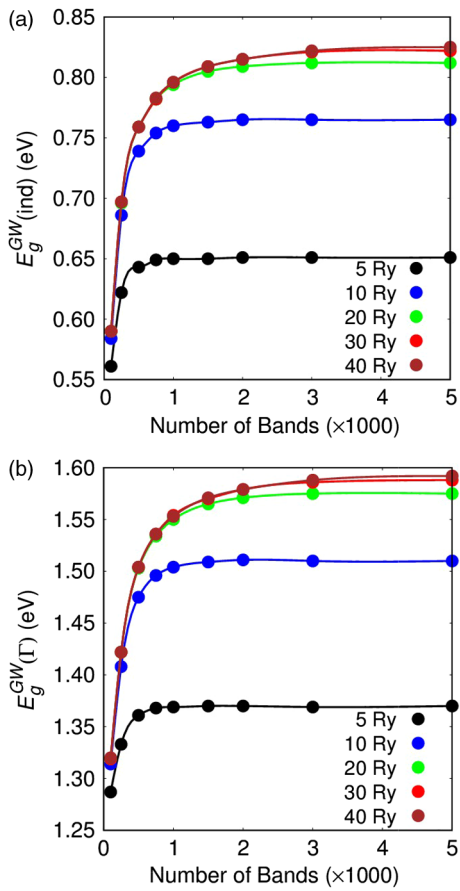


FIG. 6. Calculated quasiparticle band gap of LT phase SnSe as a function of the number of empty states included in the GW calculations and the kinetic energy cutoff for the dielectric matrices. (a) Minimum indirect band gap; (b) direct gap at the Γ point.

the dielectric function and self-energy calculations by a numerical integration on a sparse energy grid. Using this new method, we achieve a speed-up factor of about 10 times for small to medium-sized systems and up to 100 times for large systems containing hundreds of atoms [38].

C. Engineering the band-edge states through uniaxial and biaxial strains

With the above understanding at hand, we now investigate the effects of the uniaxial strain along the lattice b (zigzag, or y) and c (armchair, or z) directions [defined in Fig. 1(a)] on the electronic structure of SnSe. The crystal structures are fully relaxed under fixed strains using the optB86b functional as we discussed earlier. For uniaxial strains along the zigzag direction, the lattice constant c decreases from 4.77 to 4.17 Å as the strain along the b direction ϵ_b varies from -8% to 8% ; lattice a changes from 11.59 to 11.62 Å.

The dependence of the band gap on the uniaxial strain applied along the zigzag and armchair directions is shown in Fig. 7. For the strain applied along the zigzag direction,

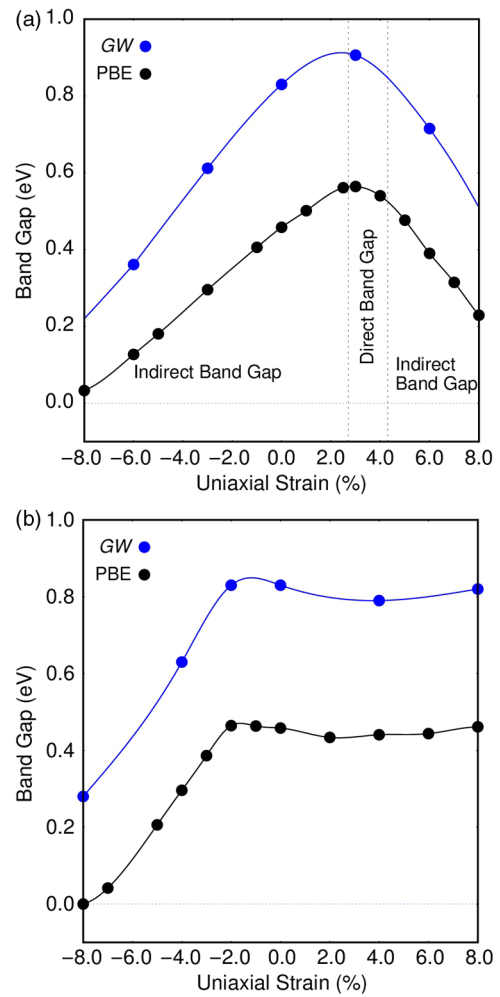


FIG. 7. Strain-dependent band gap of LT phase SnSe under uniaxial strain along (a) the zigzag (lattice b) direction and (b) the armchair (lattice c) direction. GW results are shown in blue, and PBE results in black.

the GW band gap decreases monotonically from 0.83 to 0.22 eV with compressive strains as shown in Fig. 7(a). Under tensile strains, the band gap first increases slightly, reaching a maximum value of about 0.92 eV, and then the band gap decreases with increasing strain. Perhaps more interesting is that the system becomes a direct gap material under a moderate strain ranging from about 2.5% to 4.5% as shown in Fig. 7(a). Defining the band-gap deformation potential $\alpha_e = dE_g/d\epsilon$, we get $\alpha_e = 7.8$ eV for moderate compressive strains (evaluated at around $\epsilon = -4\%$) and -6.7 eV for tensile strains (evaluated at around $\epsilon = 4\%$) along the zigzag direction. The different band-gap deformation potential under compressive and tensile strains and the indirect-to-direct band-gap transition are manifestations of the distinct wave function characteristic of the band-edge states, which respond rather differently to applied strains, as we discussed earlier.

To understand the effects of strain on the band-edge states and, therefore, the band gap, we show in Fig. 8 the

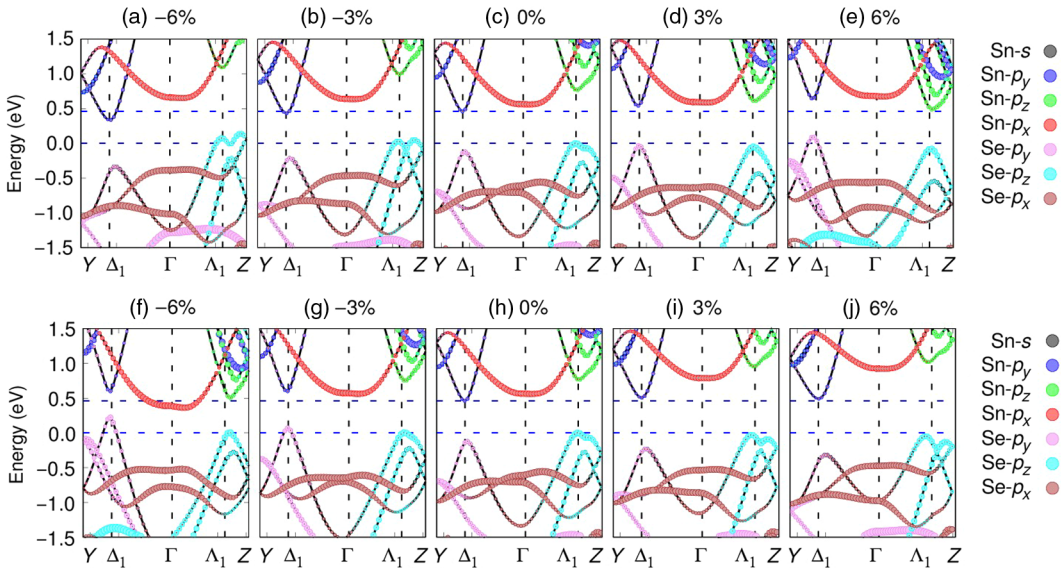


FIG. 8. Projected band structure of LT phase SnSe calculated using the PBE functional under strains along the zigzag direction (upper panels) and the armchair direction (bottom panels).

projected DFT band structures calculated with different strains; Figs. 8(a)–8(e) are for uniaxial strains along the zigzag direction, whereas Figs. 8(f)–8(j) are for strains along the armchair direction. We use the Sn semicore 4d as the reference level to align the band structures. For the strain applied along the zigzag direction, the energies of local band extrema at the Λ_1 point [labeled as states *A* and *C* in Fig. 8(c)] both move lower as the tensile strain increases. These states are derived from the Se p_z (state *A*, local VBM) and Sn p_z (state *C*, local CBM). As the strain increases, lattice *c* (*z* direction) shrinks, resulting in the lowering of the energy of these states.

In contrast, the energies of local band extrema at the Δ_1 point [labeled as states *B* and *D* in Fig. 8(c)] move higher with increasing strain along the zigzag direction. These states are derived from the Se p_y (state *B*, local

VBM) and Sn p_y (state *D*, local CBM). Note that the lattice *b* is oriented along the *y* direction as shown in Fig. 1(a). As the strain increases, states derived from the p_y orbitals move higher, whereas states derived from the p_z orbitals move lower. As a result, there is an indirect-to-direct band-gap transition at strain ranging from about 2.5% to 4.5%. The position of the CBM changes from Δ_1 to near Λ_1 beyond 4.5% tensile strain. The VBM position, which is located at Λ_1 at zero strain, moves to near Δ_1 under tensile strains greater than 2.5%. The charge densities of the four states, namely, *A*, *C*, *B*, and *D*, are shown in Fig. 9 to illustrate their atomic origins. The strain dependence of the energy of these four states is also summarized in Fig. 9.

Interestingly, the two Se p_z -derived valence states near Λ_1 (shown in cyan in the figure) respond differently

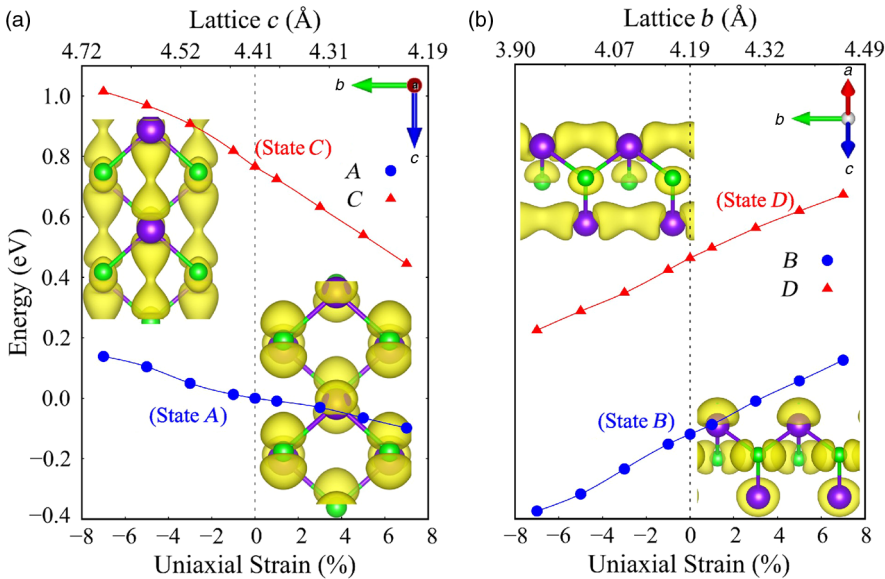


FIG. 9. Charge densities of the four local extrema labeled *A*, *C*, *B*, and *D* and their strain dependence, illustrating their distinct wave-function characters and response to lattice strains.

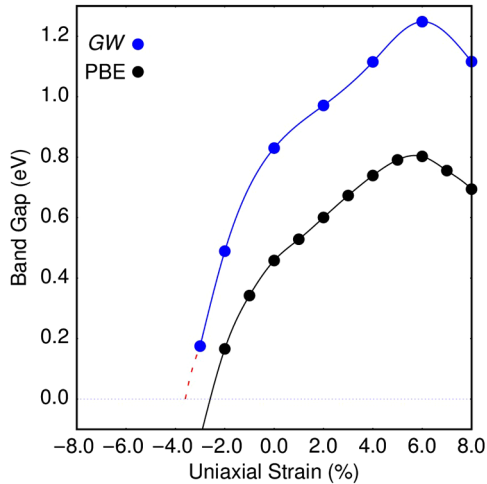


FIG. 10. Variation of the band gap of LT phase SnSe under the biaxial strain applied on the bc plane. The GW results are shown in blue, and the DFT-PBE results in black.

to strains along the zigzag direction as shown in Figs. 8(a)–8(e), presumably due to the bonding and antibonding characters of the two states. The opposite movement of the two bands results in the development of two degenerate hole valleys along the Γ -Z direction (or four hole valleys in the Brillouin zone) under about -3% compressive strain as shown in Fig. 8(b). Another remarkable feature of the strain effects on the electronic structure is the simultaneous development of multiple electron and hole valleys at around 3% of tensile strain as shown in Fig. 8(d). Strain-induced multivalley electronic structure is also predicted for uniaxial strains along the armchair direction (bottom panels in Fig. 8) and for biaxial strains as shown in Fig. 11.

We now discuss briefly the effects of strains ϵ_c along the lattice c (armchair, or z) direction. Lattice constant a changes from 11.73 to 11.43 Å, and lattice constant b changes from 4.38 to 4.08 Å as ϵ_c varies from -8% to 8% . The behavior of the strain-dependent band gap is quite different from the previous case as shown in Fig. 7(b). The band gap remains nearly constant (within 0.1 eV) when ϵ_c varies from -2% to 8% . The gap, however, decreases monotonically for compressive strains beyond -2% . Figures 8(f)–8(j) show the movement of the band-edge states under uniaxial strains along the armchair direction. Compared with Figs. 8(a)–8(e), the valence band-edge

states near Δ_1 (Se p_y derived) and Λ_1 (Se p_z) show an opposite trend. In other words, the Se p_y -derived states near Δ_1 move downward relative to the Se p_z -derived states near Λ_1 with increasing strain. As the strain increases from -8% to 8% , the position of the VBM state moves from near Δ_1 to near Λ_1 . The CBM state is of Sn p_y character for $\epsilon_c > -1.5\%$, located at Δ_1 . For $\epsilon_c < -1.5\%$, the Sn p_x -derived state becomes the CBM. It should be pointed out that DFT calculations using the PBE functional predict an insulator-metal transition when the compressive strain exceeds about -8% in both cases. Our GW results suggest, however, that such a transition happens at a much greater strain of about -11% . Therefore, extra caution must be taken when one attempts to predict an insulator-metal transition using DFT results.

Biaxial strains can be realized in experiments by growing thin-film samples on lattice mismatched substrates. The calculated band gap decreases rapidly under compressive biaxial strains applied on the b - c (or y - z) plane as shown in Fig. 10. Our results indicate that a compressive biaxial strain of less than 4% is able to induce an insulator-metal transition. The rapid closing of the band gap is a result of the reduced bonding-antibonding splitting between the hybridized Se and Sn p_x states under compressive strains as shown in Fig. 11. The lattice constant a (x direction) expands with the compressive strain, changing from 11.61 to 12.52 Å as the biaxial strain varies from 0 to -8% . Since the bonding-antibonding splitting depends strongly on the overlap between the Se and Sn p_x orbitals, the expanded a lattice greatly reduces this splitting and, thus, rapid closing of the band gap with compressive strains. Under tensile strains, the band gap first increases with increasing strain, reaching a maximum value of about 1.25 eV at a 6% tensile strain. The band gap then decreases with further increasing strain because of the downward movement of conduction Sn p_z states.

Finally, we summarize the strain-dependent number of electron or hole valleys of the $Pnma$ SnSe in Fig. 12, which may provide useful guidance for the experimental realization of band-edge state engineering through strains. We mention that the role that multivalley electronic structure plays in enhancing the thermoelectric properties [44–46] and, in general, exploiting the valley degree of freedom for various applications has generated a lot of research interest recently. Our results suggest that

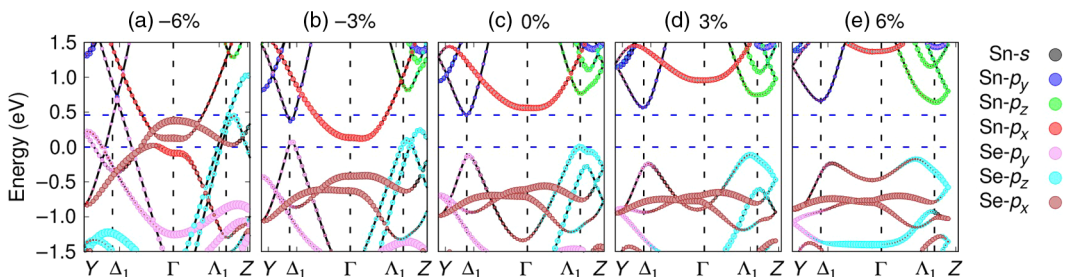


FIG. 11. Projected band structure of LT phase SnSe calculated using the PBE functional under the biaxial strain on the bc plane.

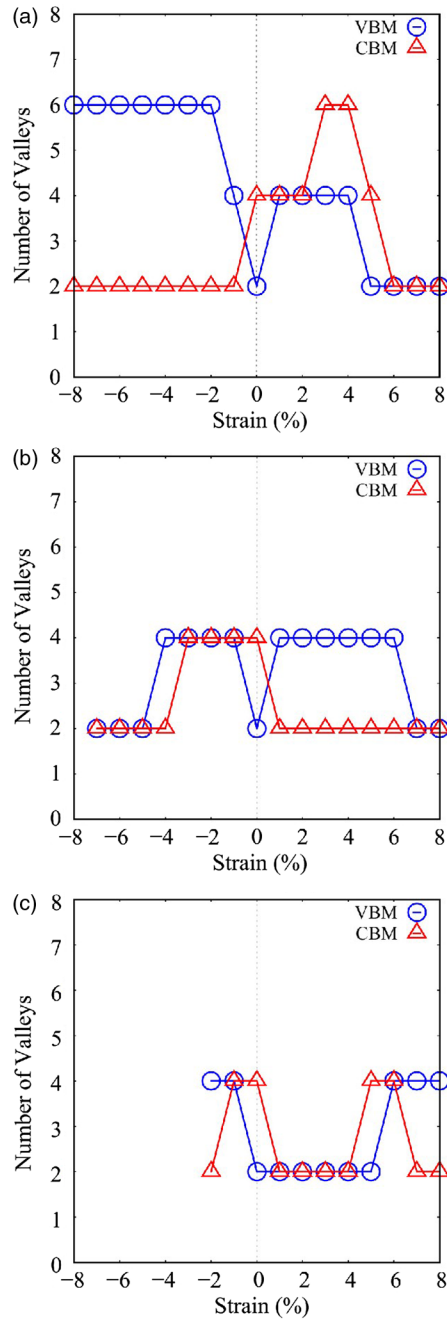


FIG. 12. Number of electron or hole valleys of the *Pnma* phase SnSe as a function of (a) strain along the zigzag (i.e., lattice *b*) direction, (b) strain along the armchair (i.e., lattice *c*) direction, and (c) biaxial strain (i.e., *bc* plane).

strains may be an effective (and active) mechanism for tuning the band-edge states to obtain multivalley electronic structures in this and other related systems. In addition, this kind of strain-induced movement of the CBM and VBM states suggests a convenient means to tune the Fermi-surface topology and to realize the Lifshitz transition [47–51] in doped SnSe. These abrupt transitions of the topology of the electron or hole pockets under strains shall have profound effects on various

thermal and transport properties of doped SnSe and deserve separate studies.

IV. CONCLUSION

Control of the near-edge electronic structure, and thus materials electronic, transport, and optical properties, is of fundamental importance for materials design and optimization for a wide range of applications. The layered structure SnSe, with its feature-rich chemical bonding, offers a unique system for strain engineering and active control of the near-edge electronic structure. Using a combined DFT and *GW* approach, we illustrate how the energy of the band-edge states with distinct atomic characters can be selectively manipulated by applying different strains. As a result, both the size and the nature (i.e., direct or indirect) of the band gap can be engineered with moderate strains. The band gap can be broadly tuned from zero to 1.2 eV. More interestingly, we propose that strain can be an effective means to realize multivalley electronic structures, providing another mechanism for optimizing SnSe for both electronic and transport applications. It is likely that the predicted strain engineering of the electronic structure will be more easily realized in experiments for structures with reduced dimensions including thin films, nanocrystals, and nanowires. The general results we present here should be applicable for these structures as long as quantum confinement does not strongly affect their electronic and structural properties.

ACKNOWLEDGMENTS

Work at SHU is supported by the National Key Basic Research Program of China (Grant No. 2015CB921600), the National Natural Science Foundation of China (No. 51672171, No. 11628407, and No. 11274222), and the Eastern Scholar Program from Shanghai Municipal Education Commission. The Special Program for Applied Research on Super Computation of the NSFC-Guangdong Joint Fund (the second phase), the supercomputing services from AM-HPC, the High Performance Computing Center at SHU, and the Center for Computational Research at UB are acknowledged. Work at UB is supported by the NSF under Grants No. DMR-1506669 and No. DMREF-1626967. Y. W. also acknowledges the support from the China Scholarship Council.

- [1] L. D. Zhao, G. Tan, S. Hao, J. He, Y. Pei, H. Chi, H. Wang, S. Gong, H. Xu, V. P. Dravid, C. Uher, G. J. Snyder, C. Wolverton, and M. G. Kanatzidis, Ultrahigh power factor and thermoelectric performance in hole-doped single-crystal SnSe, *Science* **351**, 141 (2016).
- [2] L. D. Zhao, S. H. Lo, Y. Zhang, H. Sun, G. Tan, C. Uher, C. Wolverton, V. P. Dravid, and M. G. Kanatzidis, Ultralow thermal conductivity and high thermoelectric figure of merit in SnSe crystals, *Nature (London)* **508**, 373 (2014).

- [3] K. Kutorasinski, B. Wiendlocha, S. Kaprzyk, and J. Tobola, Electronic structure and thermoelectric properties of n- and p-type SnSe from first-principles calculations, *Phys. Rev. B* **91**, 205201 (2015).
- [4] H. Zhu, W. Sun, R. Armiento, P. Lazic, and G. Ceder, Band structure engineering through orbital interaction for enhanced thermoelectric power factor, *Appl. Phys. Lett.* **104**, 082107 (2014).
- [5] J. M. Skelton, L. A. Burton, S. C. Parker, A. Walsh, C. E. Kim, A. Soon, J. Buckeridge, A. A. Sokol, C. R. Catlow, A. Togo, and I. Tanaka, Anharmonicity in the High-Temperature *Cmcm* Phase of SnSe: Soft Modes and Three-Phonon Interactions, *Phys. Rev. Lett.* **117**, 075502 (2016).
- [6] C. W. Li, J. Hong, A. F. May, D. Bansal, S. Chi, T. Hong, G. Ehlers, and O. Delaire, Orbitally driven giant phonon anharmonicity in SnSe, *Nat. Phys.* **11**, 1063 (2015).
- [7] I. Loa, R. J. Husband, R. A. Downie, S. R. Popuri, and J. W. Bos, Structural changes in thermoelectric SnSe at high pressures, *J. Phys. Condens. Matter* **27**, 072202 (2015).
- [8] Y. Zhang, S. Hao, L.-D. Zhao, C. Wolverton, and Z. Zeng, Pressure induced thermoelectric enhancement in SnSe crystals, *J. Mater. Chem. A* **4**, 12073 (2016).
- [9] J. Cao, Z. Wang, X. Zhan, Q. Wang, M. Safdar, Y. Wang, and J. He, Vertical SnSe nanorod arrays: From controlled synthesis and growth mechanism to thermistor and photo-resistor, *Nanotechnology* **25**, 105705 (2014).
- [10] F. Serrano-Sánchez, M. Gharsallah, N. M. Nemes, F. J. Mompean, J. L. Martínez, and J. A. Alonso, Record Seebeck coefficient and extremely low thermal conductivity in nanostructured SnSe, *Appl. Phys. Lett.* **106**, 083902 (2015).
- [11] S. B. Desai, G. Seol, J. S. Kang, H. Fang, C. Battaglia, R. Kapadia, J. W. Ager, J. Guo, and A. Javey, Strain-induced indirect to direct bandgap transition in multilayer WSe₂, *Nano Lett.* **14**, 4592 (2014).
- [12] A. S. Rodin, A. Carvalho, and A. H. CastroNeto, Strain-Induced Gap Modification in Black Phosphorus, *Phys. Rev. Lett.* **112**, 176801 (2014).
- [13] F. Zhang, V. H. Crespi, and P. Zhang, Prediction that Uniaxial Tension along $\langle 111 \rangle$ Produces a Direct Band Gap in Germanium, *Phys. Rev. Lett.* **102**, 156401 (2009).
- [14] N. Lu, H. Guo, L. Li, J. Dai, L. Wang, W. N. Mei, X. Wu, and X. C. Zeng, MoS₂/MX₂ heterobilayers: Bandgap engineering via tensile strain or external electrical field, *Nanoscale* **6**, 2879 (2014).
- [15] W. Ren, Y. Yang, O. Dieguez, J. Iniguez, N. Choudhury, and L. Bellaiche, Ferroelectric Domains in Multiferroic BiFeO₃ Films under Epitaxial Strains, *Phys. Rev. Lett.* **110**, 187601 (2013).
- [16] H. J. Zhao, W. Ren, X. M. Chen, and L. Bellaiche, Effect of chemical pressure, misfit strain and hydrostatic pressure on structural and magnetic behaviors of rare-earth orthochromates, *J. Phys. Condens. Matter* **25**, 385604 (2013).
- [17] M. Yang, Y. Yang, B. Hong, L. Wang, K. Hu, Y. Dong, H. Xu, H. Huang, J. Zhao, H. Chen, L. Song, H. Ju, J. Zhu, J. Bao, X. Li, Y. Gu, T. Yang, X. Gao, Z. Luo, and C. Gao, Suppression of structural phase transition in VO₂ by epitaxial strain in vicinity of metal-insulator transition, *Sci. Rep.* **6**, 23119 (2016).
- [18] T. Hu and J. Dong, Structural phase transitions of phosphorene induced by applied strains, *Phys. Rev. B* **92**, 064114 (2015).
- [19] A. J. Hatt, N. A. Spaldin, and C. Ederer, Strain-induced isosymmetric phase transition in BiFeO₃, *Phys. Rev. B* **81**, 054109 (2010).
- [20] S. Bhattacharyya and A. K. Singh, Semiconductor-metal transition in semiconducting bilayer sheets of transition-metal dichalcogenides, *Phys. Rev. B* **86**, 075454 (2012).
- [21] D. D. Cuong, S. H. Rhim, J.-H. Lee, and S. C. Hong, Strain effect on electronic structure and thermoelectric properties of orthorhombic SnSe: A first principles study, *AIP Adv.* **5**, 117147 (2015).
- [22] N. F. Hinsche, B. Y. Yavorsky, I. Mertig, and P. Zahn, Influence of strain on anisotropic thermoelectric transport in Bi₂Te₃ and Sb₂Te₃, *Phys. Rev. B* **84**, 165214 (2011).
- [23] P. Hohenberg and W. Kohn, Inhomogeneous electron gas, *Phys. Rev.* **136**, B864 (1964).
- [24] L. Hedin, New method for calculating the one-particle Green's function with application to the electron-gas problem, *Phys. Rev.* **139**, A796 (1965).
- [25] M. S. Hybertsen and S. G. Louie, Electron correlation in semiconductors and insulators: Band gaps and quasiparticle energies, *Phys. Rev. B* **34**, 5390 (1986).
- [26] R. W. Godby, M. Schlüter, and L. J. Sham, Self-energy operators and exchange-correlation potentials in semiconductors, *Phys. Rev. B* **37**, 10159 (1988).
- [27] G. Kresse and J. Hafner, Ab initio molecular dynamics for liquid metals, *Phys. Rev. B* **47**, 558 (1993).
- [28] G. Kresse and J. Furthmüller, Efficiency of ab-initio total energy calculations for metals and semiconductors using a plane-wave basis set, *Comput. Mater. Sci.* **6**, 15 (1996).
- [29] J. P. Perdew and W. Yue, Accurate and simple density functional for the electronic exchange energy: Generalized gradient approximation, *Phys. Rev. B* **33**, 8800 (1986).
- [30] J. P. Perdew, K. Burke, and M. Ernzerhof, Generalized Gradient Approximation Made Simple, *Phys. Rev. Lett.* **77**, 3865 (1996).
- [31] W. Kohn and L. J. Sham, Self-Consistent Equations Including Exchange and Correlation Effects, *Phys. Rev.* **140**, A1133 (1965).
- [32] D. M. Ceperley and B. J. Alder, Ground State of the Electron Gas by a Stochastic Method, *Phys. Rev. Lett.* **45**, 566 (1980).
- [33] S. Grimme, Semiempirical GGA-type density functional constructed with a long-range dispersion correction, *J. Comput. Chem.* **27**, 1787 (2006).
- [34] J. Klimes, D. R. Bowler, and A. Michaelides, Chemical accuracy for the van der Waals density functional, *J. Phys. Condens. Matter* **22**, 022201 (2010).
- [35] J. Klimeš, D. R. Bowler, and A. Michaelides, Van der Waals density functionals applied to solids, *Phys. Rev. B* **83**, 195131 (2011).
- [36] F. S. Ham, Dynamical Jahn-Teller Effect in Paramagnetic Resonance Spectra: Orbital Reduction Factors and Partial Quenching of Spin-Orbit Interaction, *Phys. Rev.* **138**, A1727 (1965).
- [37] J. Deslippe, G. Samsonidze, D. A. Strubbe, M. Jain, M. L. Cohen, and S. G. Louie, BerkeleyGW: A massively parallel computer package for the calculation of the quasiparticle and optical properties of materials and nanostructures, *Comput. Phys. Commun.* **183**, 1269 (2012).

- [38] W. Gao, W. Xia, X. Gao, and P. Zhang, Speeding up GW calculations to meet the challenge of large scale quasiparticle predictions, *Sci. Rep.* **6**, 36849 (2016).
- [39] A. A. Mostofi, J. R. Yates, G. Pizzi, Y.-S. Lee, I. Souza, D. Vanderbilt, and N. Marzari, An updated version of wannier90: A tool for obtaining maximally-localised Wannier functions, *Comput. Phys. Commun.* **185**, 2309 (2014).
- [40] K. Adouby, C. Perez-Vicente, and J. C. Jumas, Structure and temperature transformation of SnSe. Stabilization of a new cubic phase $\text{Sn}_4\text{Bi}_2\text{Se}_7$, *Z. Kristallogr.* **213**, 343 (1998).
- [41] G. Shi and E. Kioupakis, Quasiparticle band structures and thermoelectric transport properties of p-type SnSe, *J. Appl. Phys.* **117**, 065103 (2015).
- [42] A. K. Singh and R. G. Hennig, Computational prediction of two-dimensional group-IV mono-chalcogenides, *Appl. Phys. Lett.* **105**, 042103 (2014).
- [43] B. C. Shih, Y. Xue, P. Zhang, M. L. Cohen, and S. G. Louie, Quasiparticle Band Gap of ZnO: High Accuracy from the Conventional G(0)W(0) Approach, *Phys. Rev. Lett.* **105**, 146401 (2010).
- [44] Y. Tang, Z. M. Gibbs, L. A. Agapito, G. Li, H. S. Kim, M. B. Nardelli, S. Curtarolo, and G. J. Snyder, Convergence of multi-valley bands as the electronic origin of high thermoelectric performance in CoSb_3 skutterudites, *Nat. Mater.* **14**, 1223 (2015).
- [45] H. Tamaki, T. Kanno, A. Sakai, K. Takahashi, H. Kusada, and Y. Yamada, High thermoelectric performance in the multi-valley electronic system $\text{Zr}_3\text{Ni}_3\text{Co}_{3-x}\text{Sb}_4$ and the high-mobility $\text{Zr}_3\text{Ni}_{3-x}\text{Cu}_x\text{Sb}_4$, *Appl. Phys. Lett.* **104**, 122103 (2014).
- [46] P. Norouzzadeh and D. Vashaee, Classification of valleytronics in thermoelectricity, *Sci. Rep.* **6**, 22724 (2016).
- [47] I. M. Lifshitz, Anomalies of electron characteristics of a metal in the high pressure region, *Sov. Phys. JETP* **11**, 1130 (1960).
- [48] K. Quader and M. Widom, Lifshitz and other transitions in alkaline-earth 122 pnictides under pressure, *Phys. Rev. B* **90**, 144512 (2014).
- [49] C. Liu, T. Kondo, R. M. Fernandes, A. D. Palczewski, E. D. Mun, N. Ni, A. N. Thaler, A. Bostwick, E. Rotenberg, J. Schmalian, S. L. Bud'ko, P. C. Canfield, and A. Kaminski, Evidence for a Lifshitz transition in electron-doped iron arsenic superconductors at the onset of superconductivity, *Nat. Phys.* **6**, 419 (2010).
- [50] H. Chi, C. Zhang, G. Gu, D. E. Kharzeev, X. Dai, and Q. Li, Lifshitz transition mediated electronic transport anomaly in bulk ZrTe_5 , *New J. Phys.* **19**, 015005 (2017).
- [51] Y. Wu, N. H. Jo, M. Ochi, L. Huang, D. Mou, S. L. Bud'ko, P. C. Canfield, N. Trivedi, R. Arita, and A. Kaminski, Temperature-Induced Lifshitz Transition in WTe_2 , *Phys. Rev. Lett.* **115**, 166602 (2015).